CFD Simulations of Landing and Takeoff CRM High-Lift Configurations

Veer N. Vatsa*
NASA Langley Research Center, Hampton,VA 23681

John C. Lin †, Latunia P. Melton‡, and David P. Lockard§
NASA Langley Research Center, Hampton,VA 23681

Ryan Ferris¶
Dassault Systemes Simulia Corp., 301 E Ocean Blvd, Suite 1200, Long Beach, CA 90802

Numerical simulations have been performed for a conventional high-lift version of the Common Research Model (CRM) corresponding to landing and takeoff configurations. Computed values of lift and drag for the landing configuration are compared with the experimental data acquired in the 14- by 22-Foot Subsonic Tunnel (14×22) at the NASA Langley Research Center (LaRC). Simulations replicated the experimentally observed improvements in the lift characteristics in the presence of a nacelle chine. Flow visualization images indicate that vortices generated by the nacelle chine reduce flow separation regions on the upper surface of the wing at higher angles of attack. Based on such observations, the takeoff configuration considered is also equipped with a nacelle chine, and testing of this configuration is planned in the 14×22 tunnel in the near future. Preliminary solutions are also presented to explore the feasibility of using a localized flap-gap blowing (LFGB) active flow control concept for improving the aerodynamic performance at takeoff conditions.

Nomenclature

C_D	drag coefficient, $F_x/(0.5\rho_\infty {V_\infty}^2 S)$
C_L	lift coefficient, $F_z/(0.5\rho_\infty {V_\infty}^2 S)$
C_p	pressure coefficient, $(p-p_\infty)/(0.5\rho_\infty {V_\infty}^2)$
C_{pt}	total pressure coefficient, $(p_t-p_{t\infty})/(0.5\rho_\infty {V_\infty}^2)$
F_x	x-component of integrated force
F_z	z-component of integrated force
L/D	lift to drag ratio
p	static pressure
p_t	total pressure
Re	Reynolds number based on mean aerodynamic chord
S	wing reference area
V	total velocity
x, y, z	Cartesian coordinates
y^+	turbulence length scale
α	angle of attack
η	normalized semispan location
ρ	density

Subscripts:

∞	freestream quantity

*Senior Research Scientist, Computational AeroSciences Branch, Research Directorate; Associate Fellow AIAA
†Senior Research Scientist, Flow Physics Branch, Research Directorate; Associate Fellow AIAA
‡Senior Research Scientist, Flow Physics Branch, Research Directorate; Associate Fellow AIAA
§Senior Research Scientist, Computational AeroSciences Branch, Research Directorate; Associate Fellow AIAA
¶A&D Solution Consultant Specialist, Member AIAA

Abbreviations:

AFC	active flow control
CFD	computational fluid dynamics
CRM	Common Research Model
CRM-HL	high-lift version of Common Research Model
DNS	direct numerical simulation
FT	feed tube
FTPR	feed tube pressure ratio, $p_{t_{FT}}/p_\infty$
HL	high-lift
LaRC	Langley Research Center
LBM	Lattice Boltzmann Method
LFGB	Localized Flap-Gap Blowing
MAC	mean aerodynamic chord
NASA	National Aeronautics and Space Administration
SHL	simplified high-lift
3-D	three-dimensional
VLES	very large eddy simulation
VR	variable resolution

I. Introduction

The high-lift systems of modern transport aircraft that cruise at transonic speeds are designed to provide adequate lift at slower speeds during takeoff and landing operations [1]. The high-speed version of the Common Research Model (CRM) was developed jointly by Boeing and NASA for applied computational fluid dynamics (CFD) validation studies [2, 3]. The initial high-lift version of the CRM model, known as the CRM-HL, was designed by Lacy and Sclafani [4] to provide a relevant modern airplane geometry set that could be made available in the public domain for collaboration with academia, industry and government agencies. More recently, two variants of the CRM-HL rigging (gaps, overhangs, slat and flap angles) configurations have been tested in the low-speed tunnels at landing and takeoff conditions [5–7]. CFD validation research will benefit greatly from the data generated from such wind tunnel tests.

Lin et al. [7, 8] conducted wind tunnel tests on the 10% scale model of the CRM-HL in the landing configuration at the 14- by 22-Foot Subsonic Tunnel (14×22) of the NASA Langley Research Center (LaRC). Several variants of the model were tested to establish a target or reference for comparison with an active flow control (AFC) enabled simplified high-lift (CRM-SHL-AFC) model. In addition, the effect of the nacelle/pylon and a nacelle chine on aerodynamic performance was documented. As demonstrated by Vatsa et al. [9, 10], CFD played an important role in supporting the wind tunnel tests by conducting parametric studies prior to testing.

The current paper focuses on CFD simulations of the landing and the takeoff configurations of the CRM-HL over a broad angle-of-attack range, and compares the resulting solutions with experimental data when feasible. Limited comparisons for the landing configuration without the chine were presented in Ref. [10]. Results for the landing configuration with the chine will be presented in this paper to demonstrate the effect of a chine on aerodynamic forces and the flowfield as a function of angle of attack. Computed lift and drag coefficients for the landing configuration will be compared with the experimental data of Lin et al. [7, 8] to demonstrate the accuracy of the CFD for computing flow over complex high-lift configurations over a broad angle-of-attack range.

One of the main reasons for undertaking simulations for the takeoff configuration is to provide CFD support for an upcoming project, where drag reduction techniques using AFC will be explored. In this paper we examine the feasibility of using localized flap-gap blowing (LFGB) to improve the lift to drag ratio of the CRM-HL takeoff configuration. Results obtained with the initial version of LFGB AFC modules will be presented here, including the flowfield inside the actuators and the effect of AFC on flow behavior on the flaps. Potential modification to the LFGB modules will be considered after careful examination of the effect of the current AFC modules on the surrounding flowfield.

II. Configuration and Computational Setup

The geometries under consideration correspond to variants of the 10%-scale, semispan, high-lift configurations that are based on the "open" NASA Common Research Model (CRM) [2, 3]. The conventional CRM-HL configuration, shown in Fig. 1, is based on the design of Lacy and Sclafani [4]. It consists of wing, fuselage, nacelle/pylon, slats and flaps, where the slats and flaps are attached to the main wing by slat and flap brackets, respectively. For the original, baseline landing configuration, the slat and flap deflections are set at 30° and 37°, respectively, and the nominal slat and flap positions were set based on recommendation by Lacy and Sclafani [4]. An optimized reference landing configuration was defined in Ref. [5], but will not be considered in this work. However, the optimized takeoff condition defined in Ref. [5] will be used for the LFGB investigation. In this case, the slat and flap deflections are 22° and 25°, respectively. In contrast with the landing configuration, the trailing edge gap of the slats is sealed for the takeoff configuration.

The semispan of the wing is 115.675 inches, and the mean aerodynamic chord in the stowed (cruise) configuration is 27.58 inches at a span station of 46.875 inches. The wing reference area (S) used for normalizing force coefficients is 2973.6 square inches. Computations are performed with the model enclosed in the test section to facilitate a direct comparison with the experimental data acquired in the solid-wall tunnel. A simplified approach is used for modeling the wind tunnel for the in-tunnel simulations, where the test article is enclosed inside the rectangular test section of the wind tunnel. The CRM model is installed on top of a 3.5-inch-thick peniche (standoff), (see Fig. 1), to reduce the effect of tunnel floor boundary layer on the test article. The peniche is attached to a turntable that can be rotated to change the angle of attack (α) of the model relative to the incoming stream. No-slip (viscous) boundary conditions are imposed on the tunnel floor, the peniche, and all of the exposed solid surfaces. The test section for simulations is extended in the upstream region such that the computed boundary-layer thickness at the entrance of the physical test section is in good agreement with the measurements at that location. The computational box was also extended in the downstream region beyond the physical test section to reduce the effect of downstream boundary condition. Slip (inviscid) boundary conditions are imposed on the tunnel ceiling and side walls. Velocity and temperature are imposed on the tunnel inflow boundary. Static pressure is specified at the exit plane of the test section for the downstream boundary condition, and total pressure is specified at the feed-tube inlets for the AFC cases.

III. Simulation Method

Numerical simulations presented in this paper have been performed using the PowerFLOW® code, which is a compressible flow solver based originally on the three-dimensional 19-state (D3Q19) Lattice Boltzmann Method (LBM). The PowerFLOW® code represents LBM-based CFD technology developed over the last 30 years [11–15], and has been extensively validated for a wide variety of applications ranging from academic direct numerical simulation (DNS) cases to industrial flow problems in the fields of aerodynamics [16] and aeroacoustics [17]. In contrast to methods based on the classical Navier-Stokes (N-S) equations, the LBM uses a simpler and more general physics formulation at the mesoscopic level [11]. As shown in Refs. [18, 19], the LBM equations recover the macroscopic hydrodynamics of the Navier-Stokes equations through the Chapman-Enskog expansion.

The PowerFLOW® code can be used to solve the Lattice Boltzmann equation in a DNS mode [20], where all of the turbulent scales are spatially and temporally resolved. However, the DNS mode is very compute intense, and because of compute resource considerations, this approach is not practical for Reynolds numbers beyond 10,000 or so. Therefore, for most engineering problems at high Reynolds numbers (>10,000), the simulations are usually conducted in conjunction with a hybrid turbulence modeling approach where the smaller scales are modeled and larger, energy-containing scales are directly resolved. For the current work, the Lattice Boltzmann Very Large Eddy Simulation (LB-VLES) approach described in Refs. [13], [14] and [21] is used. All of the results presented here were simulated with the compressible version of the PowerFLOW® code [22–24].

The PowerFLOW® code is used for solving the Lattice Boltzmann equation on embedded Cartesian meshes, which are generated within the PowerFLOW® Software Suite. Variable Resolution (VR) regions can be defined to allow for local mesh refinement by successive factors of two in each direction [11]. To reduce the resolution requirement near solid surfaces for high Reynolds number flows, a hybrid wall function is used to model the near-wall region of the boundary layer [16, 25]. The PowerFLOW® code uses explicit time marching to solve the governing equations and scales efficiently on modern computer clusters consisting of thousands of processors, making it suitable for large-scale applications.

IV. Results

The computations of the three-dimensional (3-D) flowfields for the CRM-HL landing and takeoff configurations enclosed within the 14×22 test section have been performed using the compressible version of the PowerFLOW® code. As mentioned in the previous section, the computations are performed on embedded Cartesian meshes, which are generated within the PowerFLOW® Software Suite. Finer resolution was specified for high-gradient regions, such as the suction surface of the slats, the main wing, and the flaps. A total of 13 VR regions were used for the present simulations. Based on previous experience with the PowerFLOW® code [26], the minimum spacing normal to viscous surfaces was chosen to produce an average value of 120 for y^+. In the current work, additional VR regions similar to the ones reported in Ref. [9] were also created to capture the vortical regions emanating from the slat side edges, the fuselage/wing and nacelle/pylon junctures, and the wing tip.

Since the flowfield is inherently unsteady, the computations are run long enough in time for the flow to achieve a quasisteady state, as determined by the variation of the integrated forces (e.g., lift) in time for a given case. Computations are typically run for a physical time of 0.5-0.6 seconds, which corresponds to the time required for traveling a distance of approximately 50 chord lengths. This allows us to extract time-averaged solutions for the integrated forces, surface pressures and streamlines, and to make quantitative comparisons among different configurations and flow conditions.

A. Landing configuration

An attempt is made here to assess the accuracy of the PowerFLOW® code for predicting the lift and drag coefficients for the CRM-HL configurations over a broad angle-of-attack (α) range, including the maximum lift condition, being fully aware that computing the flow near maximum lift is a very challenging task for CFD methods even today [27]. The simulations for the landing configuration were performed at a freestream Mach number of 0.2, and a Reynolds number of 3.27 million based on the mean aerodynamic chord (MAC) of the model, corresponding to the test conditions in the 14×22 at NASA Langley Research Center. The simulations were performed for this configuration with and without the nacelle chine to assess the effect of the chine on the aerodynamic performance. The computational grid consisted of approximately 436 million voxels (cells) for the case without the chine, and 453 million voxels when the chine is added to the nacelle.

A comparison of the computed and measured lift coefficients as a function of angle of attack (α) is presented in Fig. 2 for the landing configuration. It should be noted that the CFD simulations included the test section walls, therefore, the experimental data used for comparison were without any wall corrections applied. All of the results presented here agree quite well in the linear range ($\alpha \leq 12^\circ$), indicating that the chine has very little effect on the lift levels for this range of α. The dip in the lift curve at $\alpha = 14^\circ$ is eliminated when the chine is present, a trend that is also replicated by the CFD results. Except for a slight overprediction, the computed results compare quite well with the measured data in the linear range of $\alpha \leq 12^\circ$ for both configurations. The computed results replicate the lift curve for the chine case quite accurately up to maximum lift conditions of $\alpha = 17^\circ$. However, the CFD slightly underpredicts the maximum lift for the configuration without the chine.

The drag coefficients for these cases are compared in Fig. 3. Once again, all of the results are in good agreement for ($\alpha \leq 12^\circ$), similar to what was observed for the lift curves in Fig. 2. The measured values of drag are slightly higher for the chine case for $\alpha > 12^\circ$, and the overall agreement between the CFD and measured data is quite good, except in the stall region. The most noticeable differences between the computed results and experimental data are observed for the no chine case starting at $\alpha = 15^\circ$, and for the chine case starting at $\alpha = 17^\circ$. These results are very encouraging, considering the various uncertainties incurred during simulation of such a complex configuration in a wind tunnel environment.

1. Sectional pressure comparisons

Time-averaged surface pressure coefficient (C_p) distributions were extracted at the sectional cuts of the model corresponding to the spanwise rows of pressure taps shown in Fig. 4. Each spanwise row of ports was defined with the flaps and slats retracted, so the ports are not coplanar when the high-lift devices are deployed. The experimental data were acquired at a discrete number of pressure taps placed along these rows. The computed values of C_p are compared with the measured data at the nominal landing approach angle of attack, $\alpha = 8^\circ$, and near the maximum lift condition at $\alpha = 16^\circ$. These comparisons are presented in Figs. 5 and 6 at the inboard (y=27.75 inches, $\eta = 0.240$) and outboard (y=63.8 inches, $\eta = 0.552$) midflap span stations, respectively, for the landing configuration with and without the nacelle chine. In these figures, the results for the slat were shifted upstream by approximately 1.2 inches to avoid overlap between the slat and main wing leading edge regions.

The computational results are in good agreement with the measured data at both the inboard and outboard

midflap stations, and the effect of increasing the angle of attack is well predicted over most of the slat, wing, and flap surfaces. Increasing the angle of attack from 8° to 16° results in much higher values of suction pressure on the upper surface, especially in the vicinity of the slat and wing leading edges, resulting in higher lift. Adding the nacelle chine results in increased suction pressures in the vicinity of the slat and flap leading edges at both the inboard and the outboard stations, although the effect is more pronounced at the inboard station for the $\alpha = 16°$ case. The chine also produces a slightly higher suction peak on the inboard section of the main wing, especially at the higher angle of attack, resulting in higher lift. These effects are captured very accurately by the simulations, as seen in Figs. 5 and 6. Other than slight overpredictions of the slat leading edge suction peaks, and underprediction of suction peaks at the flap leading edge, especially for the chine case, the computed pressure distributions agree quite well with the measured data.

2. Flow visualization

The suction surface streamlines and skin-friction contours based on time-averaged solutions are presented here for $\alpha = 8°$ and 16° to assess the effect of the chine on surface flow patterns at moderate and high angles of attack. The results based on the time-averaged solutions are compared in Fig. 7 for $\alpha = 8°$, and in Fig. 8 for $\alpha = 16°$. Based on the results presented in Fig. 7, the chine seems to have a negligible effect on the surface flow patterns for the $\alpha = 8°$ case. However, that is not the case at the higher angle of attack of 16°. In the absence of the chine, a low skin-friction wedge-shaped region develops, starting at the nacelle/pylon juncture, as shown in Fig. 8 (a). The streamline pattern indicates the presence of a reversed flow pocket in that region. Adding the chine practically eliminates the low skin-friction area and the reversed flow pocket (Fig. 8 (b)), which contributes to the additional lift observed in Fig. 2.

Total pressure, C_{pt}, contours at several streamwise sections are presented in Fig. 9 for the $\alpha = 8°$ case. The negative C_{pt} values indicate total pressure losses (pressure deficit) that are mainly due to near wall viscous effects, or due to off-surface wake effects. As reported by Koklu et al. [28], several sets of vortices originating from the inboard/outboard slat cutouts, nacelle/pylon juncture and strake leading edge are observed for the baseline (no chine) case. Other than the presence of an additional vortex generated by the chine (see Fig. 9 (b), the chine has only a minimal effect on the flowfield at this moderate angle of attack. However, the chine has a more significant effect on the vortex patterns at the higher angle of attack ($\alpha = 16°$), as seen in Fig. 10. Most notably, a much stronger controlling vortex is generated by the chine that persists all the way up to the trailing edge region of the wing. This vortex pushes down the vortex that originates from the nacelle/pylon juncture.

B. Takeoff configuration

The CRM-HL takeoff configuration is made up of the same high-lift components as the landing configuration discussed in the previous section. The main difference is in the slat and flap deflection angles. Based on the recommendation of Lacy and Clark [5], a slat deflection of 22°, and a flap deflection of 25° were chosen for the takeoff configuration. In addition, the gap between slat trailing edge and main wing leading edge was sealed as suggested in Ref. [5]. Because the nacelle chine has been shown to improve the performance of both, the landing and the takeoff configurations at higher angles of attack [6], all of the results presented here for the takeoff configuration included the chine in the simulations. Computations were performed at a freestream Mach number of 0.26, and a Reynolds number of 4.24 million based on the MAC of the 10% scale wind tunnel model. These correspond to the baseline conditions reported in Ref. [6], and also the conditions proposed for future testing of the takeoff configuration in the NASA's 14×22 facility. A limited set of simulations have been performed so far on the baseline grid for the takeoff configuration, and these results are discussed in the following paragraphs.

The computed lift variation for the takeoff configuration with angle of attack (α) is compared with the results obtained for the landing configuration (with chine) in Fig. 11. The lift coefficients for the takeoff configuration are smaller compared to the landing configuration results at a given α, which is attributed to the fact that smaller slat and flap deflection angles are employed for the takeoff configuration. The overall trends observed here for the lift curves are qualitatively similar to the ones reported in the QuinetiQ wind tunnel test [6]. However, the maximum lift occurs at a lower α compared to what was reported in Ref. [6], where the results were corrected for wall interference. Keeping in mind the fact that wall corrections can increase the equivalent α by about 1.5° at maximum lift for such configurations, the current predictions are considered in line with the expected trends.

Surface skin-friction contours and streamline patterns for $\alpha = 8°$ and 14° are compared in Fig. 12. Low skin friction and reversed flow regions are observed near the flap trailing edge at both angles of attack. Regions of lower skin-friction levels are also observed near the wing root juncture and on the outboard portion of the wing

at the higher angle ($\alpha = 14^\circ$), i.e. close to the maximum lift conditions. The streamline patterns shown in Fig. 12 (b) clearly indicate flow separation near the outboard wing trailing edge, similar to what was observed for the landing configuration at higher α in Fig. 8. The total pressure contours corresponding to these surface flow patterns are shown in Fig. 13. As expected, the vortices generated from the slat side edges, nacelle/pylon, strake leading edge, and chine are more prominent and much stronger at the higher angle of attack. The strake vortex is much stronger for takeoff compared with landing, and the vortices from the nacelle/slat tips are weaker. The loading distribution is obviously different because of the changes in deployment angles.

C. Localized flap gap blowing (LFGB)

A joint numerical/experimental study is planned under the sponsorship of the NASA Advanced Air Transport Technology (AATT) project to explore localized applications of AFC to reduce drag. One candidate application is the localized flap gap blowing concept (LFGB) for enhancing the aerodynamic performance of the the CRM-HL takeoff configuration. The primary goal is to increase the lift-to-drag (L/D) ratio with minimal changes to the baseline wing configuration. As an initial effort in this direction, AFC modules were added along the three flap brackets, and a top view of this arrangement is shown in Fig. 14. Four probes were added to collect flowfield data along the feed-tube paths of the inboard and the middle flap actuators, marked in this figure as pt1-pt4. As seen in Fig. 14, the feed-tube path for the outboard actuator is much shorter, and only three probes were used for that actuator. The feed tubes are routed through existing openings in the main spar that had been used for the CRM-SHL-AFC configuration. Numerical simulations were performed for varying levels of feed-tube input pressure. Flowfield data from the simulations were collected at these probes and at the inlet faces of the feed tubes to compare results for different levels of input pressure.

Total pressure and Mach number variation along the actuator paths are presented in Figs. 15 and 16 for the feed-tube input pressure ratios (FTPR) of 2.0 and 2.5. where the FTPR is defined as the ratio of the total pressure at the feed-tube inlet and the free stream pressure. The feed-tube inlet is designated as probe 0 in these figures. The total pressure drops slightly at probes 1 and 2, and a steep drop in pressure levels is observed from probe 2 to 3 for the inboard actuator. This is mainly due to the fact that the feed-tube diameter for the inboard actuator corresponding to probe 3 location is larger compared to the upstream locations. By contrast, a more gradual pressure drop is seen for the middle actuator. Increasing the input pressure levels shifts these curves to higher levels. The Mach number for the inboard actuator grows almost linearly from inlet to probe 3, and then goes through a sudden drop at probe 4 near the nozzle exit. Although our intent was to place the probe 4 at the nozzle exit plane, closer examination of the configuration indicated that this probe was located slightly downstream of the nozzle exit, and hence the velocity is lower at that location for the inboard actuator. On the other hand, the Mach number shows a monotonic increase from inlet to the nozzle exit throughout the actuator path for the middle AFC module, the highest velocity being at the nozzle exit. The flow behavior in the outboard actuator was similar to the middle actuator, and the exit velocity at the outboard actuator nozzle was slightly higher compared to the middle actuator.

1. Effect of LFGB on Flow Field

Flow visualization images are presented in this section to understand the effect of the LFGB AFC concept on the surface and off-surface flowfields. The simulated surface streamline patterns on the upper surface of the LFGB configuration are compared in Fig. 17 for the AFC case run using FTPR=2.5 with the baseline AFC-OFF case. The effect of AFC is very small and localized in small regions (denoted by small elliptical regions on Fig. 17) near the flap leading edge along the three flap brackets. It is difficult to see any significant effect of AFC in this figure, other than the increased levels of skin friction on the flaps in the vicinity of the nozzle exits. To get a better idea of the effect of AFC, Figs. 18 (a)-(b) show zoomed views of the rectangular regions denoted in Figs. 17 (a)-(b). This rectangular region includes the nozzle exits of the middle and outboard actuators and the outboard flap. Higher skin-friction levels and reduced reversed flow regions in the vicinity of the middle and outboard actuators are clearly visible in Fig. 18 (b) for the FTPR=2.5 case. However, the effect of the LFGB AFC on the overall global flowfield is very small.

Next we present the results showing the effect of the LFGB AFC on the off-surface flowfield. The velocity (Mach) contours and the streamline patterns at a spanwise cut along the inboard flap bracket actuator are compared in Figs. 19 (a) and (b) for the AFC-Off and AFC with FTPR=2.5. Higher velocity regions are clearly visible in the feed tube and the actuator nozzle for the AFC case. However, the momentum imparted from this actuator is not sufficient to make a visible change to the flowfield over the flap leading edge and its vicinity. Similar flow patterns are presented in Figs. 20 (a) and (b) for the spanwise cut through the middle flap bracket

actuator. The velocity of the flow exiting this actuator is much higher, and the increased momentum helps reduce the off-body separation over the flap in the presence of AFC using FTPR=2.5. Although not presented here, similar results were obtained for the outboard actuator.

2. Assessment of current LFGB concept

Based on the results obtained so far, it is clear that the effect of LFGB is very localized, and it does not have much impact on the global flowfield. Examination of the integrated forces also indicated that the effect of the current LFGB was very minimal on total lift and drag forces. It is worth mentioning that average mass flow through each actuator is approximately 0.05 lb/sec at FTPR=2.5 through the feed tubes for each actuator in the current LFGB design. By contrast, it required approximately 0.45 lb/sec on the inboard flap and 0.6 lb/sec on outboard flap for CRM-SHL to produce a lift increment of $20 - 25\%$ to recover the lift corresponding to CRM-HL (see Ref. [10]) by reducing the extent of reversed flow region on a highly deflected flap. By comparison, the conventional CRM-HL configuration has been optimized to reduce the extent of separation, and achieving a $1 - 2\%$ increment in lift by cleaning up the flow near flap brackets should require significantly less mass flow for AFC. Nonetheless, the LFGB modules will have to be redesigned to pump more mass flow through the actuators to have a significant impact on the flowfield over the flaps to attain the desired level of lift increment. One way to increase the mass flow through LFGB actuators would be to use larger feed tubes and exit nozzles. Distribution of the flow exiting the actuator nozzle over a broader area would be more effective. The modified design should also minimize sharp turns in the feed tubes to reduce internal pressure loss, and will have to be compatible with the hardware limitations of the baseline configuration. We will also have to explore the use of higher pressure ratio input for the actuators. The current simulations were performed with the high subsonic version of the PowerFLOW® code, and based on the resulting velocities observed inside the actuator feed tubes and exit nozzles, the maximum Mach number was well within the acceptable range for the high subsonic mode for FTPR ≤ 2.5. However, significant regions of transonic flow are expected for cases where higher pressure ratio is imposed at the feed-tube inlets, and it is recommended to use the transonic version of the PowerFLOW® code for such cases.

V. Concluding Remarks

Computational results based on numerical simulations performed using the compressible Lattice Boltzmann formulation in the PowerFLOW® CFD code are presented here for the conventional high-lift CRM landing and takeoff configurations. The primary difference between these two configurations is their slat and flap deflection angles. Also, the free stream Mach and Reynolds numbers are slightly higher for the takeoff configuration.

Good agreement of numerical solutions with the measured data was obtained for the lift and drag coefficients over a broad angle-of-attack range for the landing configuration. The effect of the chine on the integrated forces was also predicted accurately, including the elimination of a lift degradation near $\alpha = 14^\circ$, that was observed in the baseline configuration without the chine. Surface and off-surface flow patterns have been presented to improve our understanding of the effects of α and the chine on the flow physics. The computed surface pressure distributions were shown to compare well with the measurements at both inboard and outboard span stations for the landing configuration.

Computational results were also presented here for the baseline takeoff configuration. The resulting lift for the takeoff configuration was compared with the landing configuration results for a broad angle of attack range. These solutions were found to be in line with the previously reported experimental results for such configurations. Surface and off-surface flow patterns were compared at nominal angles of attack for takeoff mode, and at an angle of attack corresponding to maximum lift condition. As expected, the extent of reversed flow regions on the wing and the flaps increases with an increase in angle of attack. These results will serve as a reference for assessing the effect of localized flap-gap blowing (LFGB) AFC concept for lift-to-drag ratio enhancement during takeoff mode. Preliminary results obtained for the LFGB configuration indicated that the initial design did not have a significant impact on the global flowfield and integrated forces, and design modifications to enhance the effectiveness of AFC are being explored.

Acknowledgments

This work was supported by the NASA Advanced Air Vehicles Program through the Advanced Air Transport Technology Project. The first author would like to express his appreciation to Jared Fell of the design team for providing the geometry definition for the CRM takeoff configuration including the LFGB modules, and to Scott

Brynildsen of GEOLAB for creating a watertight geometry suitable for CFD simulations.

References

[1] Van Dam, C., "The Aerodynamic Design of Multi-Element High-Lift Systems for Transport Airplanes," *Progress in Aerospace Sciences*, Vol. 38, 2002, pp. 101–144. Doi: 10.1016/S0376-0421(02)00002-7.

[2] Vassberg, J., DeHaan, M., Rivers, M., and Wahls, R., "Development of a Common Research Model for Applied CFD Validation Studies," AIAA Paper 2008-6919, August 2008. Doi: 10.2514/6.2008-6919.

[3] NASA Common Research Model, URL: http://commonresearchmodel.larc.nasa.gov, last accessed, July 2020.

[4] Lacy, D., and Sclafani, A., "Development of the Common Research Model (HL-CRM): A Representative High Lift Configuration for Transonic Transports," AIAA Paper 2016-0308, January 2016. Doi: 10.2514/6.2016-0308.

[5] Lacy, D., and Clark, A., "Definition of Initial Landing and Takeoff Reference Configurations for the High Lift Common Research Model (CRM-HL," AIAA Paper 2020-2771, June 2020. Doi: 10.2514/6.2020-2771.

[6] Evans, A., Lacy, D., Smith, I., and Rivers, M., "Test Summary of the NASA Semi-Span High-Lift Common Research Model at the QinetiQ 5-Meter Low-Speed Wind Tunnel," AIAA Paper 2020-2770, June 2020. Doi: 10.2514/6.2020-2770.

[7] Lin, J., Melton, L., Hannon, J., Andino, K. M., M.Y., Paschal, K., and Vatsa, V., "Wind Tunnel Testing of Active Flow Control on High Lift Common Research Model," AIAA Paper 2019-3723, June 2019. Doi: 10.2514/6.2019-3723.

[8] Lin, J., Melton, L., Hannon, J., Andino, M., Koklu, M., Paschal, K., and Vatsa, V., "Testing of High-Lift Common Research Model with Integrated Active Flow Control," *Journal of Aircraft*, Vol. 57, No. 6, 2020, pp. 1121–1133. Doi: 10.2514/1.C035906.

[9] Vatsa, V., Duda, B., Lin, J., Melton, L., Lockard, D., O'Connell, M., and Hannon, J., "Comparative Study of Active Flow Control Strategies for Lift Enhancement of a Simplified High-Lift Configuration," AIAA Paper 2019-3724, June 2019. Doi: 10.2514/6.2019-3724.

[10] Vatsa, V., Lin, J., Melton, L., Lockard, D., and Ferris, R., "CFD and Experimental Data Comparisons for Conventional and AFC-Enabled CRM High-Lift Configurations," AIAA Paper 2020-2939, June 2020. Doi: 10.2514/6.2020-2939.

[11] Chen, H., "Volumetric Formulation of the Lattice Boltzmann Method for Fluid Dynamics: Basic Concept," *Physical Review A*, Vol. 58, 1998, pp. 3955–3963. Doi: 10.1103/PhysRevE.58.3955.

[12] Chen, H., Teixeira, C., and Molvig, K., "Realization of Fluid Boundary Conditions via Discrete Boltzmann Dynamics," *Intl. J. Mod. Phys. C*, Vol. 9, No. 8, 1998, pp. 1281–1292. Doi: 10.1142/S0129183198001151.

[13] Yakhot, V., and Orszag, S., "Renormalization Group Analysis of Turbulence. I. Basic Theory," *J. Sci. Comput.*, Vol. 1, No. 2, 1986, pp. 3–51. Doi: 10.1007/BF01061452.

[14] Chen, H., Kandasamy, S., Orszag, S., Shock, R., Succi, S., and Yakhot, V., "Extended Boltzmann Kinetic Equation for Turbulent Flows," *Science*, Vol. 301, No. 5633, 2003, pp. 633–636. Doi: 0.1126/science.1085048.

[15] Chen, S., and Doolen, G., "Lattice Boltzmann Method for Fluid Flows," *Ann. Rev. Fluid Mech.*, Vol. 30, 1998, pp. 329–364. Doi:10.1146/annurev.fluid.30.1.329.

[16] Fares, E., and Nölting, S., "Unsteady Flow Simulation of a High-Lift Configuration using a Lattice Boltzmann Approach," AIAA Paper 2011-869, January 2011. Doi: 10.2514/6.2011-869.

[17] Khorrami, M., Fares, E., and Casalino, D., "Towards Full-Aircraft Airframe Noise Prediction: Lattice-Boltzmann Simulations," AIAA Paper 2014-2481, June 2014. Doi: 10.2514/6.2014-2481.

[18] Chen, H., Chen, S., and Matthaeus, W., "Recovery of the Navier-Stokes Equations Using a Lattice-gas Boltzmann Method," *Physical Review A*, Vol. 45, 1992, pp. 5339–5342. Doi: 10.1103/PhysRevA.45.R5339.

[19] Qiana, Y. H., D'Humieŕes, D., and Lallemand, P., "Lattice BGK Models for Navier-Stokes Equations," *Europhysics Letters*, Vol. 17, 1992, pp. 479–484. Https://iopscience.iop.org/article/10.1209/0295-5075/17/6/001/meta.

[20] Li, Y., Shock, R., and Chen, H., "Numerical Study of Flow Past an Impulsively Started Cylinder by Lattice Botzmann Method," *J. Fluid Mech.*, Vol. 519, 2004, pp. 273–300. Doi: 10.1017/S0022112004001272.

[21] Chen, H., Orszag, S., Staroselsky, I., and Succi, S., "Expanded Analogy between Boltzmann Kinetic Theory of Fluid and Turbulence," *J. Fluid Mech.*, Vol. 519, 2004, pp. 301–314. Doi: 10.1017/S0022112004001211.

[22] Shan, X., Yuvan, X.-F., and Chen, H., "Kinetic Theory Representation of Hydrodynamics: a Way Beyond the Navier-Stokes Equation," *Journal of Fluid Mechanics*, Vol. 550, 2006, pp. 413–441. Doi: 10.1017/S0022112005008153.

[23] Zhuo, C., Zhong, C., Li, K., Xiong, S., Chen, X., and Cao, J., "Application of Lattice Boltzmann Method to Simulation of Compressible Turbulent Flow," *Commun. Comput. Physics*, Vol. 8, 2010, pp. 1208–1223. Doi: 10.4208/cicp.300110.070510a.

[24] Fares, E., Wessels, M., Li, Y., Gopalakrishnan, P., Zhang, R., Sun, C., Gopalaswamy, N., Roberts, P., Hoch, J., and Chen, H., "Validation of a Lattice Boltzmann Approach for Transonic and Supersonic Simulations," AIAA Paper 2014-0952, January 2014. Doi: 10.2514/6.2014-0952.

[25] Fares, E., "Unsteady Flow Simulation of the Ahmed Reference Body using a Lattice Boltzmann Approach," *Comput. Fluids*, Vol. 35, No. 8-9, 2006, pp. 940–950. Doi: 10.1016/j.compfluid.2005.04.011.

[26] Fares, E., Duda, B., Ribeiro, A., and König, B., "Scale-resolving Simulations using Lattice Boltzmann-based Approach," *CEAS Aeronautical Journal*, Vol. 9, 2018, pp. 721–733. Doi: 10.1007/s13272-018-0317-0.

[27] Rumsey, C., Slotnick, J., and Sclafani, A., "Overview and Summary of the Third AIAA High Lift Prediction Workshop," *Journal of Aircraft*, Vol. 56, No. 2, 2019, pp. 621–644. Doi: 10.2514/1.C034940.

[28] Koklu, M., Lin, J., Hannon, J., Melton, L., Andino, M., Paschal, K., and Vatsa, V., "Investigation of the Nacelle/Pylon Vortex System on the High-Lift Common Research Model," *AIAA Journal*, 2021. Doi: 10.2514/1.J059869.

Fig. 1 Global view of the conventional high-lift CRM configuration in the 14x22 wind tunnel.

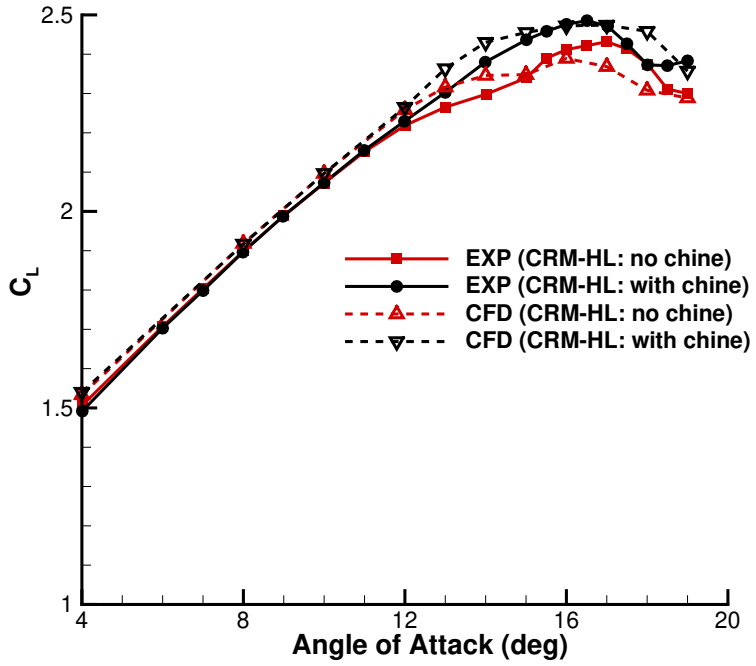

Fig. 2 Lift coefficient variation with angle of attack for CRM-HL landing configuration, Mach=0.2, $Re = 3.27 \times 10^6$.

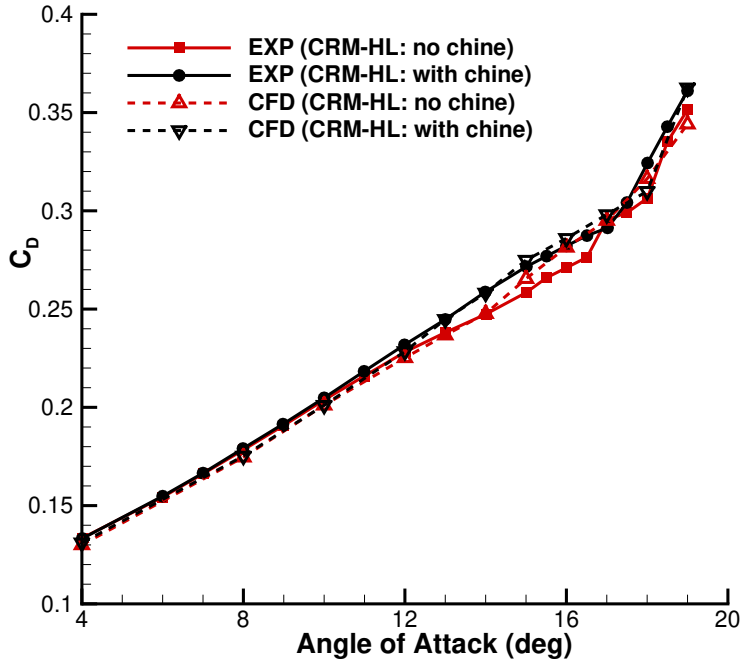

Fig. 3 Drag coefficient variation with angle of attack for CRM-HL landing configuration, Mach=0.2, $Re = 3.27 \times 10^6$.

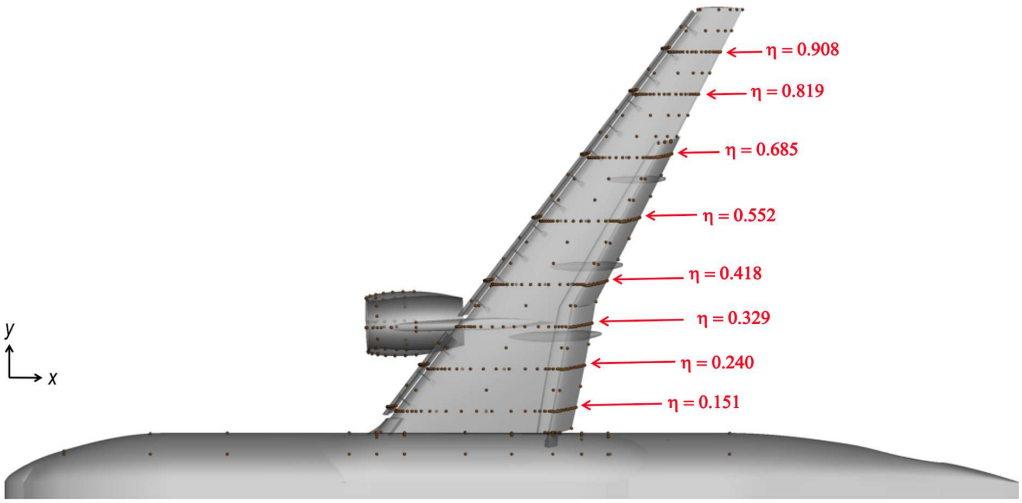

Fig. 4 Schematic of spanwise cuts aligned with pressure taps.

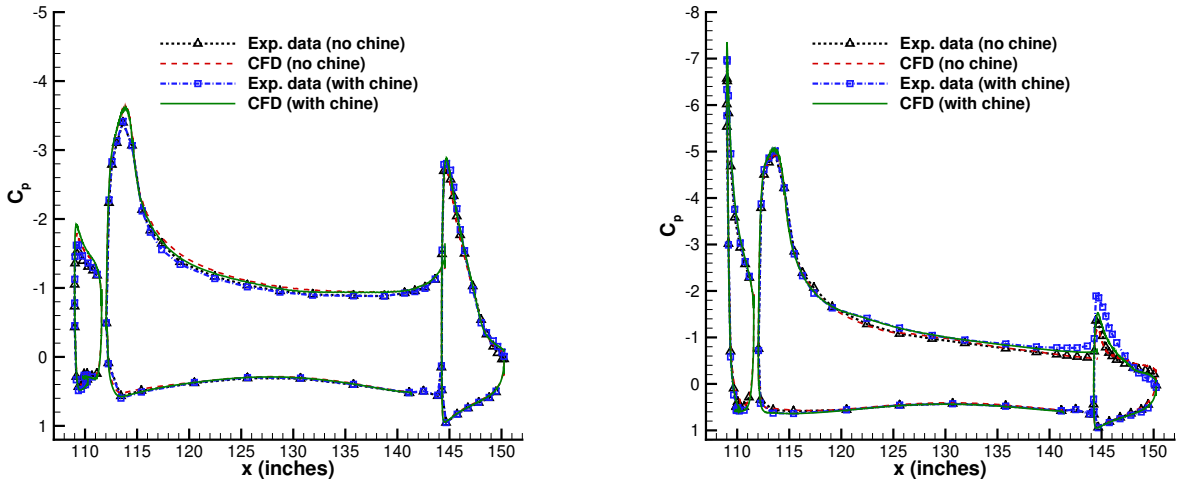

(a) $\alpha = 8°$ (b) $\alpha = 16°$

Fig. 5 Effect of chine on sectional C_p for landing configuration at y=27.75 inches ($\eta = 0.240$), Mach=0.2, $Re = 3.27 \times 10^6$.

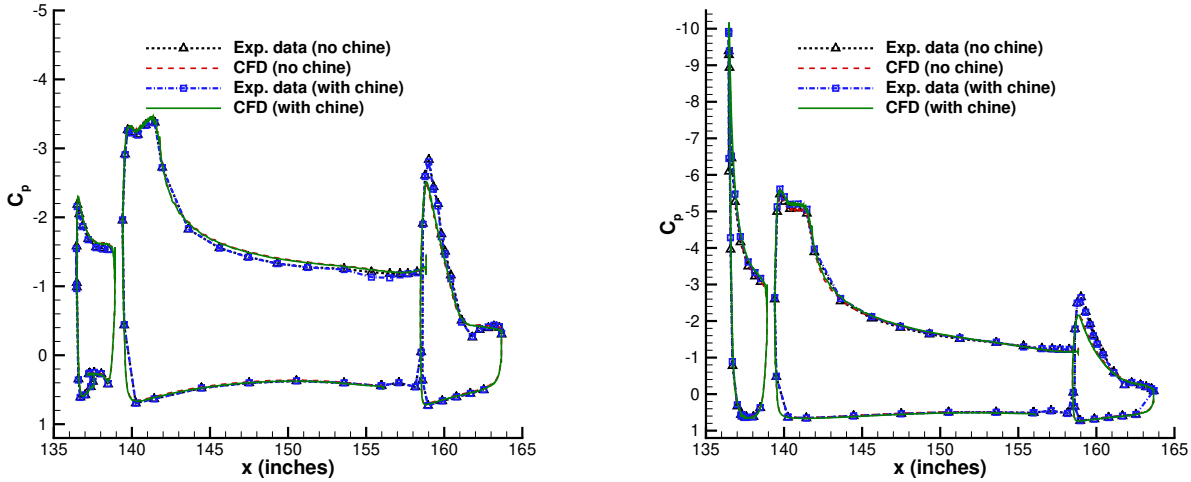

(a) $\alpha = 8°$ (b) $\alpha = 16°$

Fig. 6 Effect of chine on sectional C_p for landing configuration at y=63.8 inches ($\eta = 0.552$), Mach=0.2, $Re = 3.27 \times 10^6$.

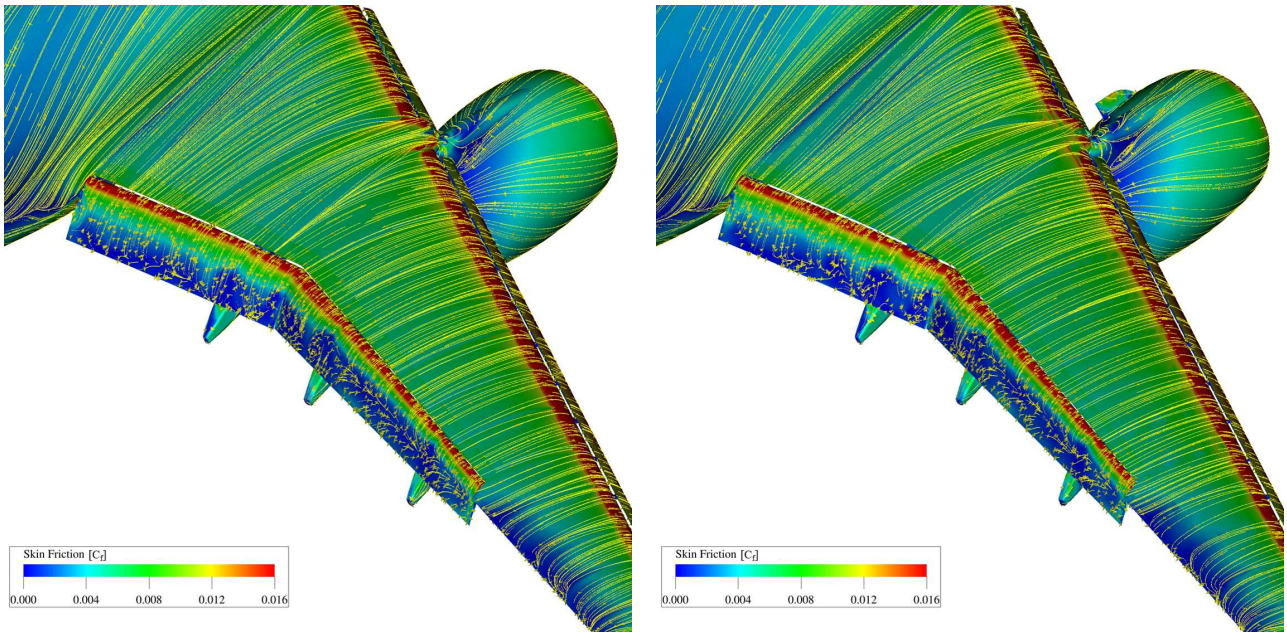

(a) No chine (b) With chine

Fig. 7 Effect of chine on simulated surface streamline patterns of landing configuration, Mach=0.2, $Re = 3.27 \times 10^6, \alpha = 8°$.

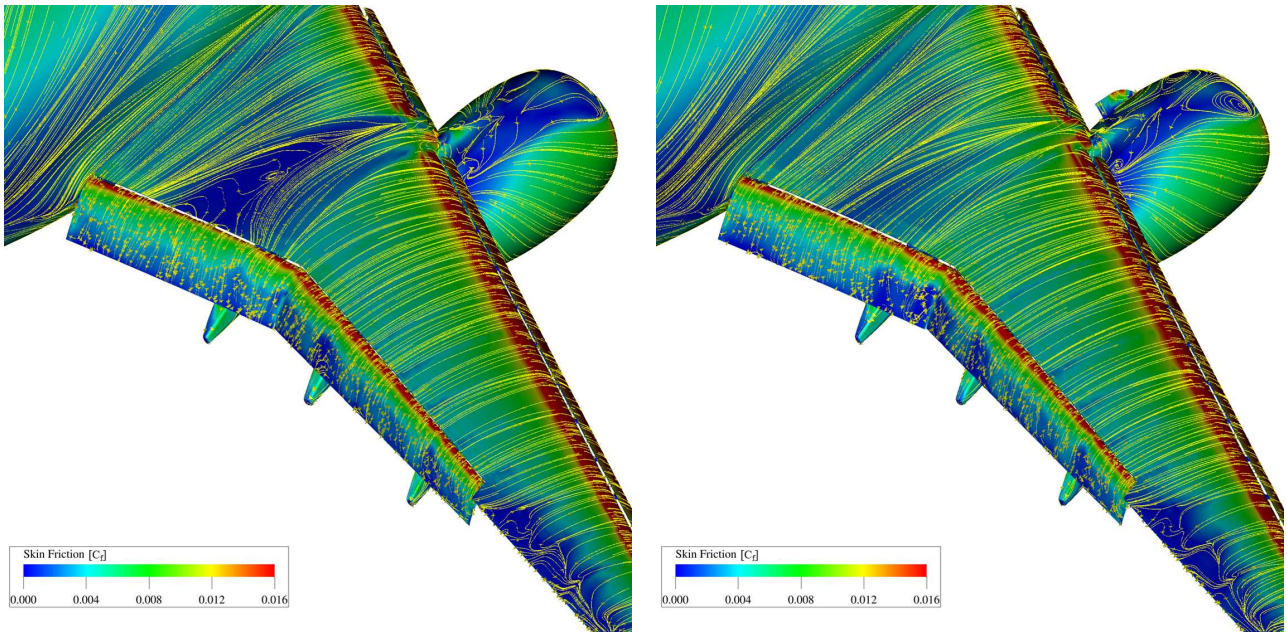

(a) No chine (b) With chine

Fig. 8 Effect of chine on simulated surface streamline patterns of landing configuration, Mach=0.2, $Re = 3.27 \times 10^6, \alpha = 16°$.

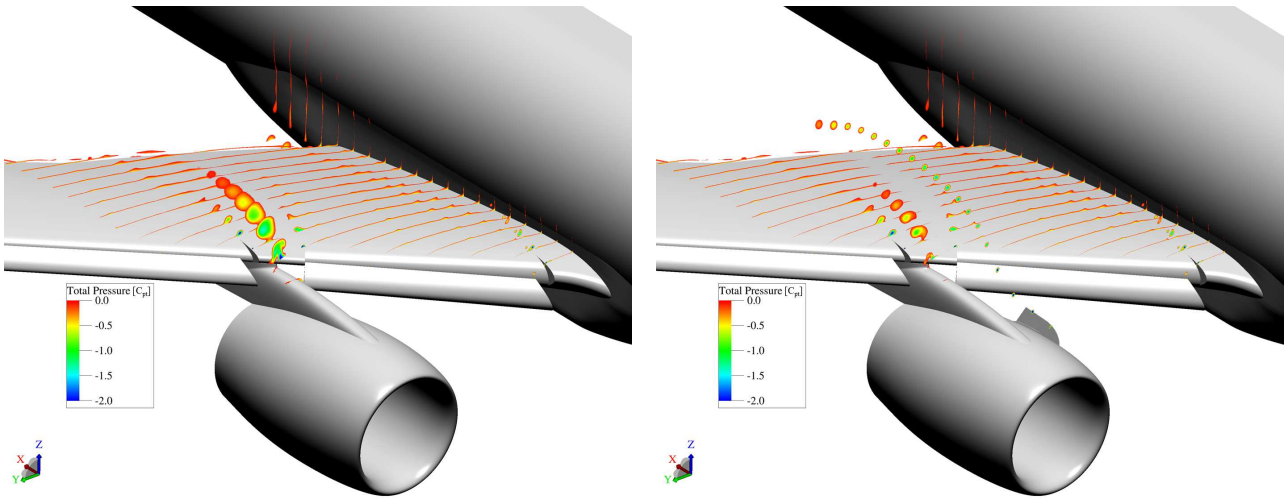

(a) No chine (b) With chine

Fig. 9 Effect of chine on C_{pt} contours at streamwise cuts of landing configuration, Mach=0.2, $Re = 3.27 \times 10^6, \alpha = 8°$.

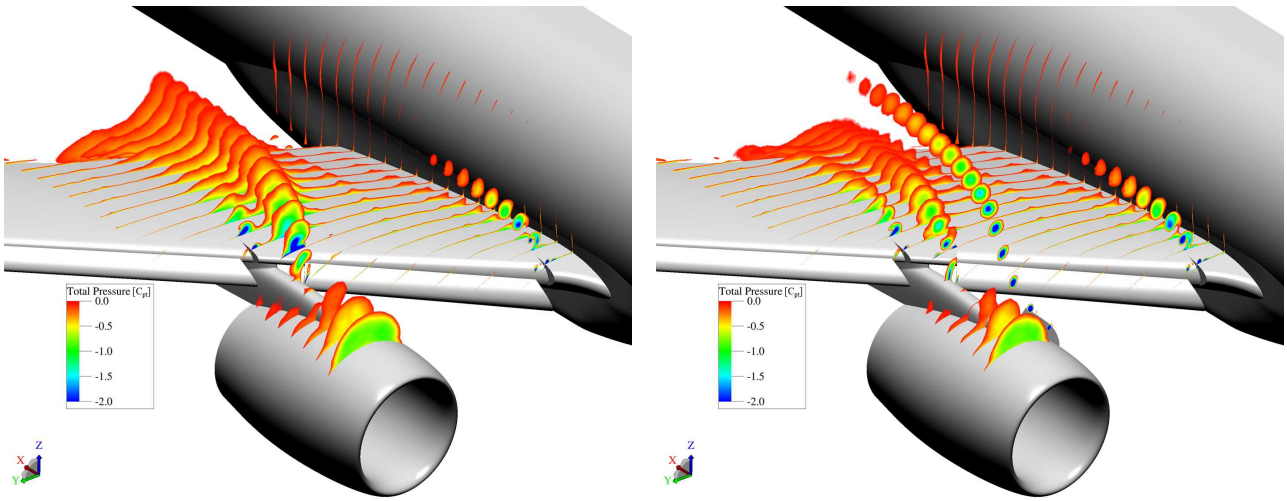

(a) No chine (b) With chine

Fig. 10 Effect of chine on C_{pt} contours at streamwise cuts of landing configuration, Mach=0.2, $Re = 3.27 \times 10^6, \alpha = 16°$.

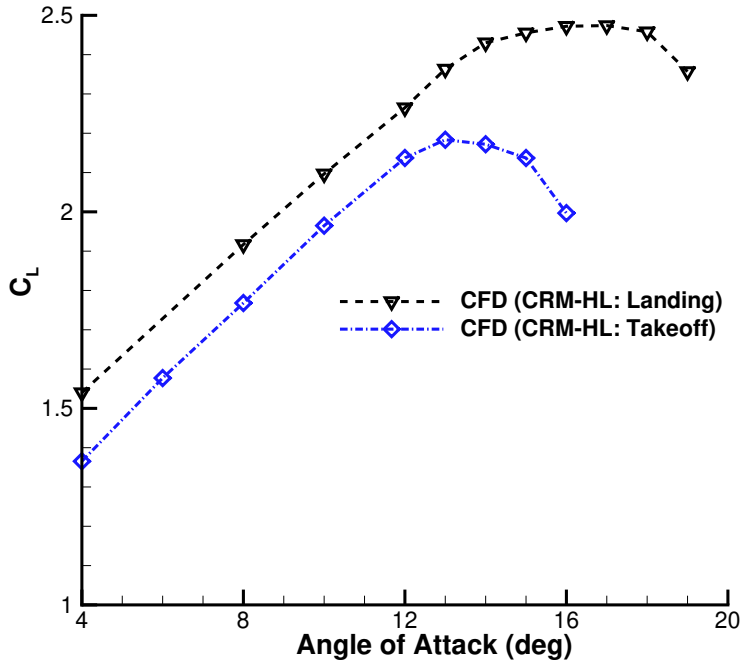

Fig. 11 Lift coefficient comparison for CRM-HL landing and takeoff configurations.

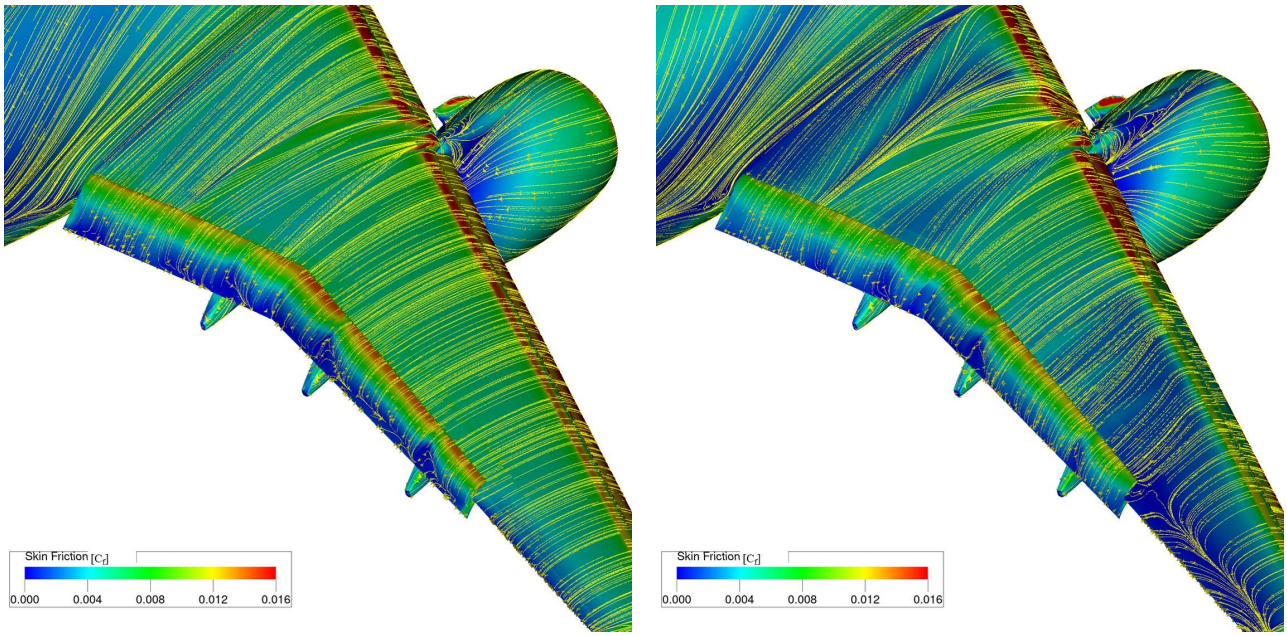

(a) $\alpha = 8°$ (b) $\alpha = 14°$

Fig. 12 Effect of α on simulated surface streamline patterns of takeoff configuration, Mach=0.26, $Re = 4.24 \times 10^6$.

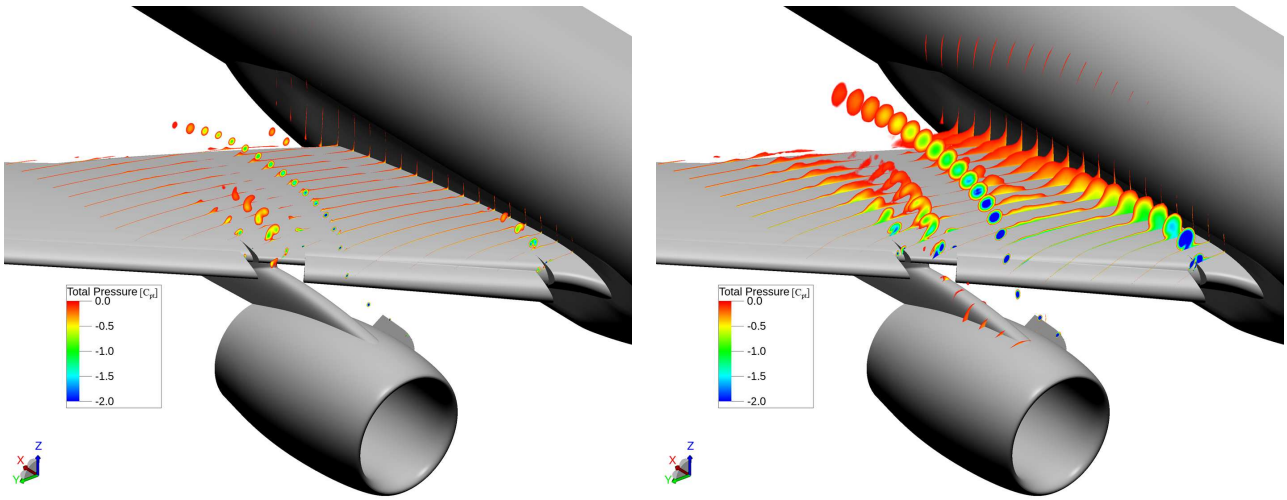

(a) $\alpha = 8°$ (b) $\alpha = 14°$

Fig. 13 Effect of α on C_{pt} contours at streamwise cuts of takeoff configuration, Mach=0.26, $Re = 4.24 \times 10^6$.

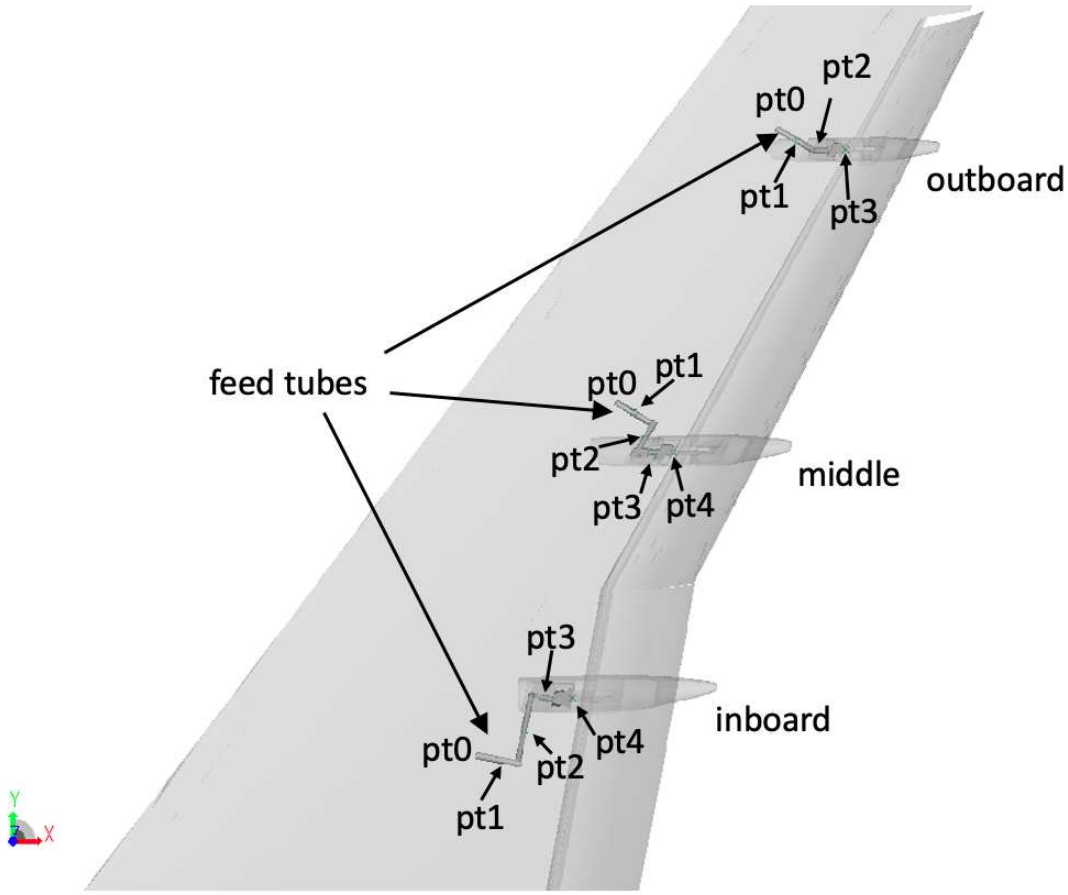

Fig. 14 Top view of AFC modules for CRM takeoff configuration.

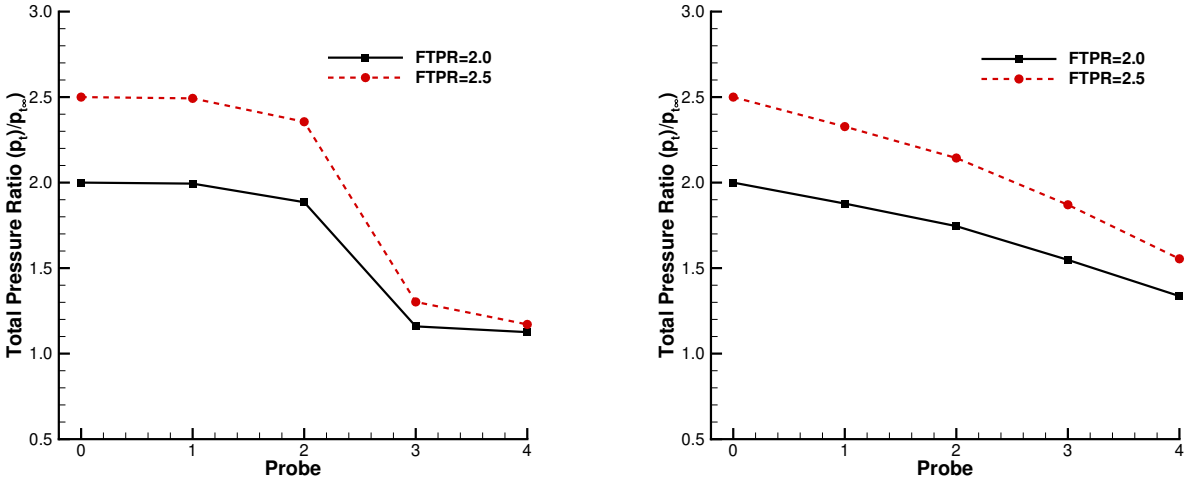

(a) inboard (b) middle

Fig. 15 Comparison of total pressure variation in feed tubes, Mach=0.26, $\alpha = 8°, Re = 4.24 \times 10^6$.

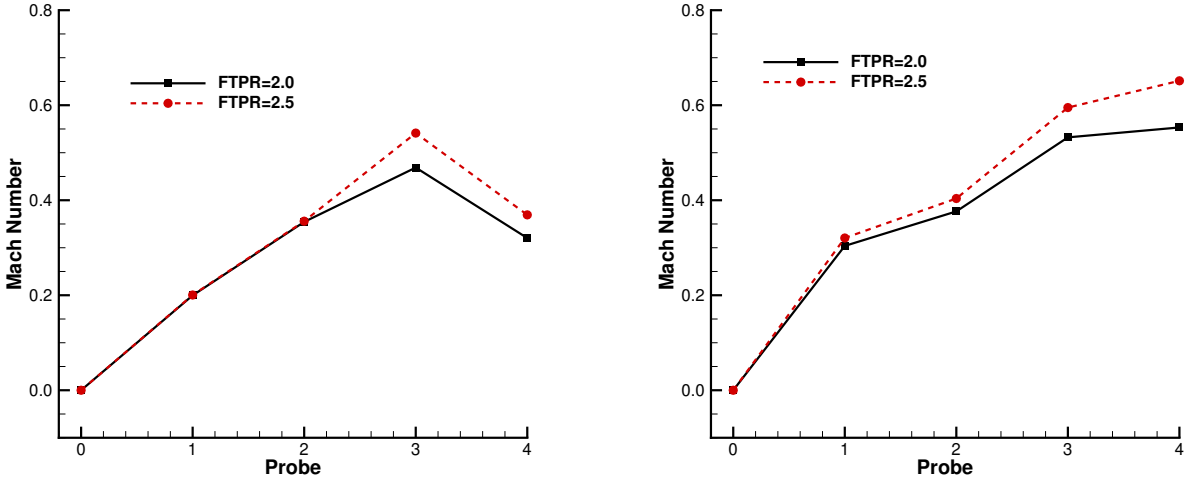

(a) inboard (b) middle

Fig. 16 Comparison of Mach number variation in feed tubes, Mach=0.26, $\alpha = 8°, Re = 4.24 \times 10^6$.

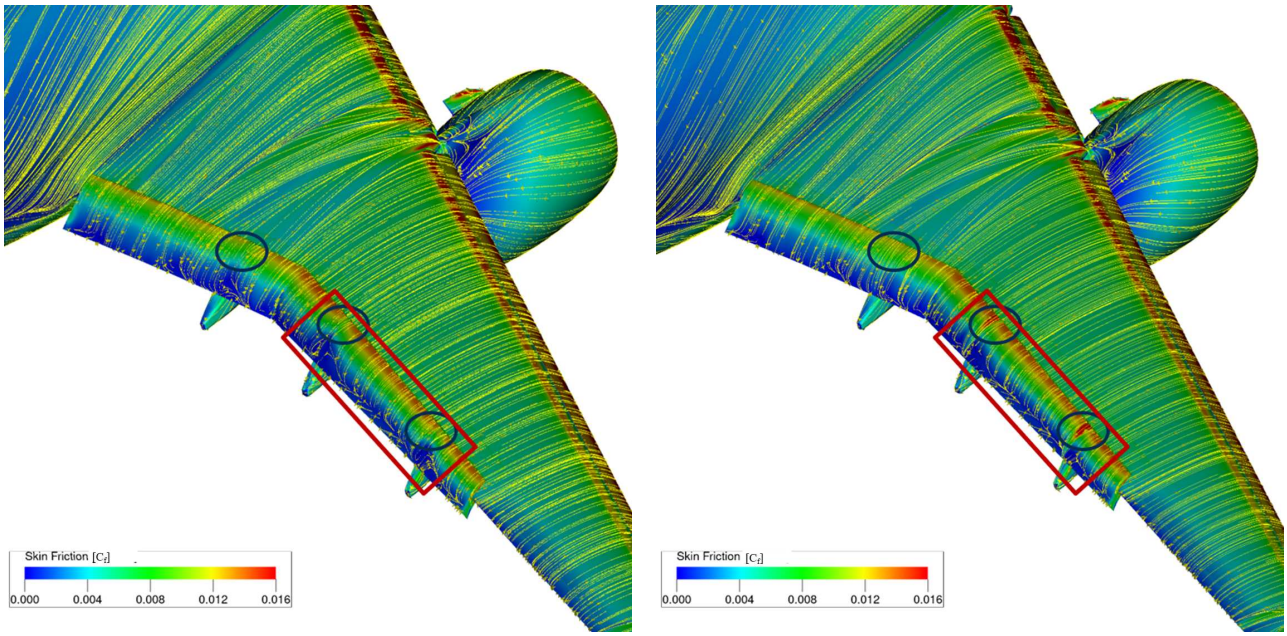

(a) AFC-OFF (b) AFC: FTPR=2.5

Fig. 17 Effect of LFGB AFC on surface flowfield of CRM configuration: global view, Mach=0.26, $\alpha = 8°, Re = 4.24 \times 10^6$.

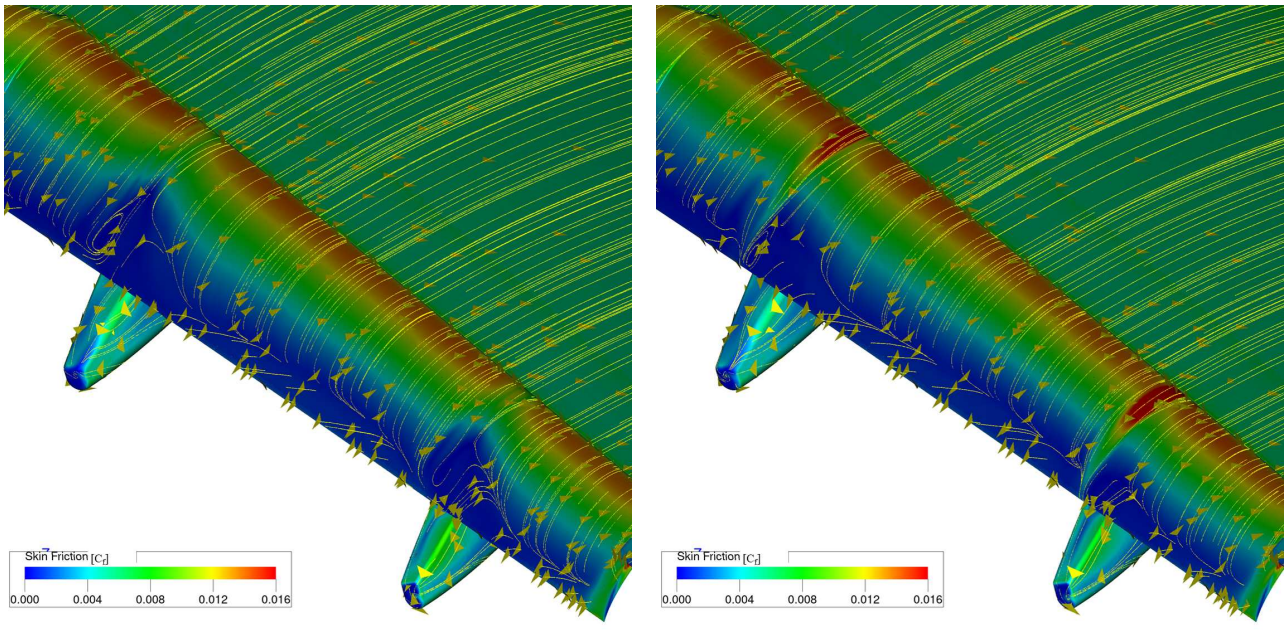

(a) AFC-OFF (b) AFC: FTPR=2.5

Fig. 18 Effect of LFGB AFC on surface flowfield of CRM configuration: zoomed view, Mach=0.26, $\alpha = 8°, Re = 4.24 \times 10^6$.

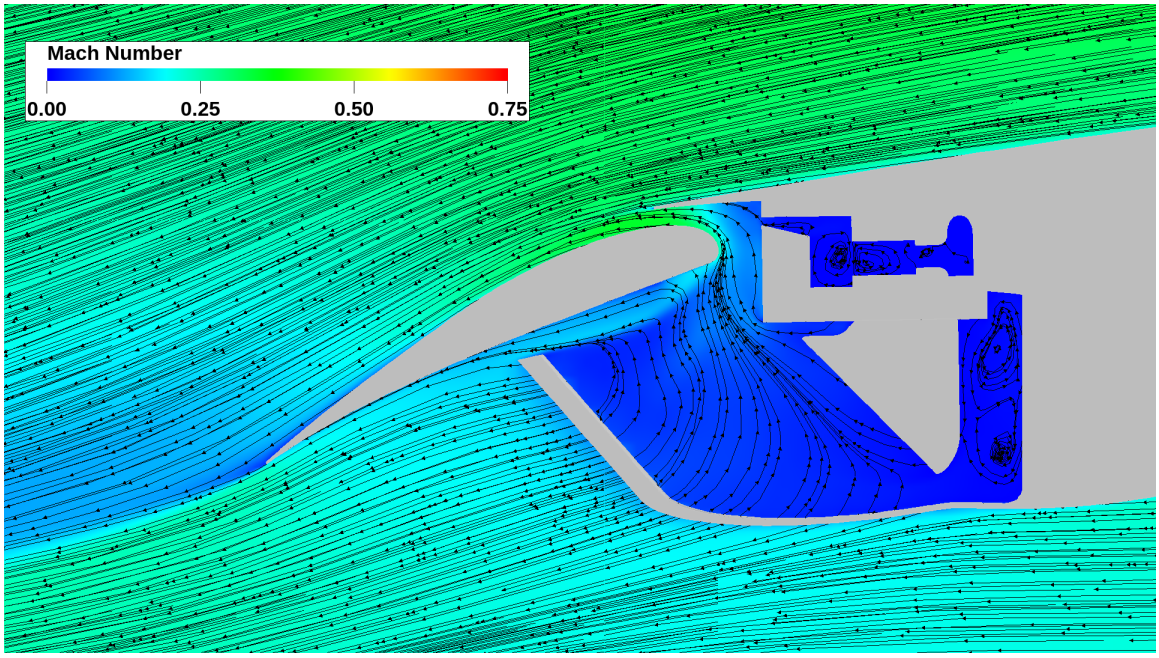

(a) AFC-OFF

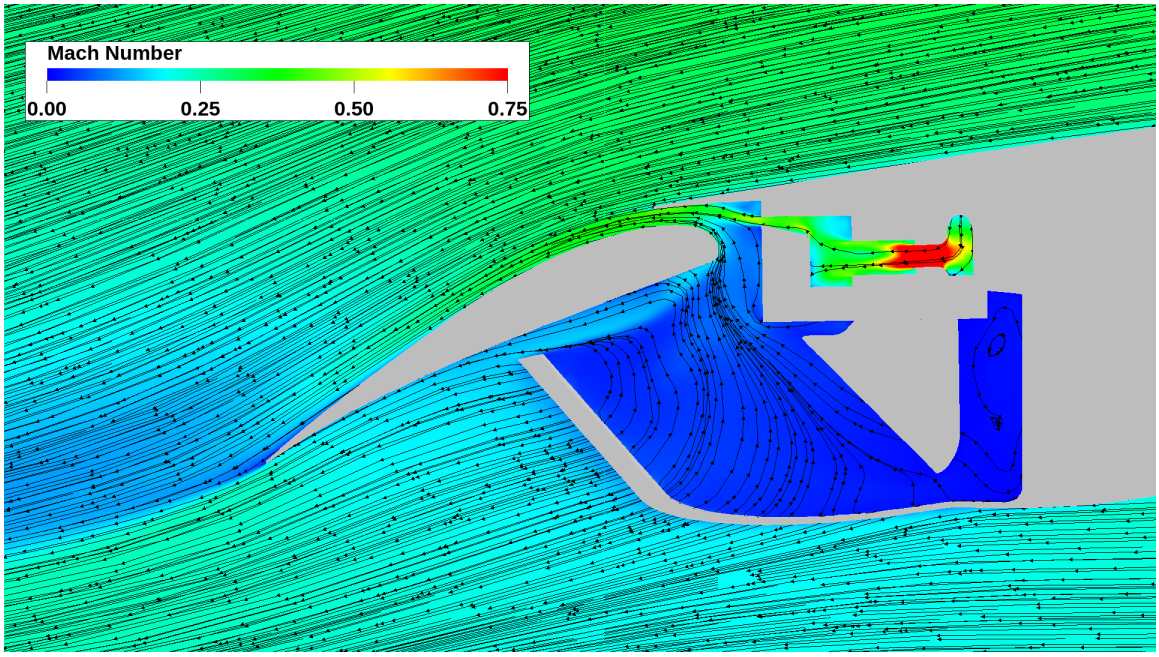

(b) AFC: FTPR=2.5

Fig. 19 Effect of LFGB AFC on off-surface flowfield at inboard section, Mach=0.26, $\alpha = 8°$, $Re = 4.24 \times 10^6$.

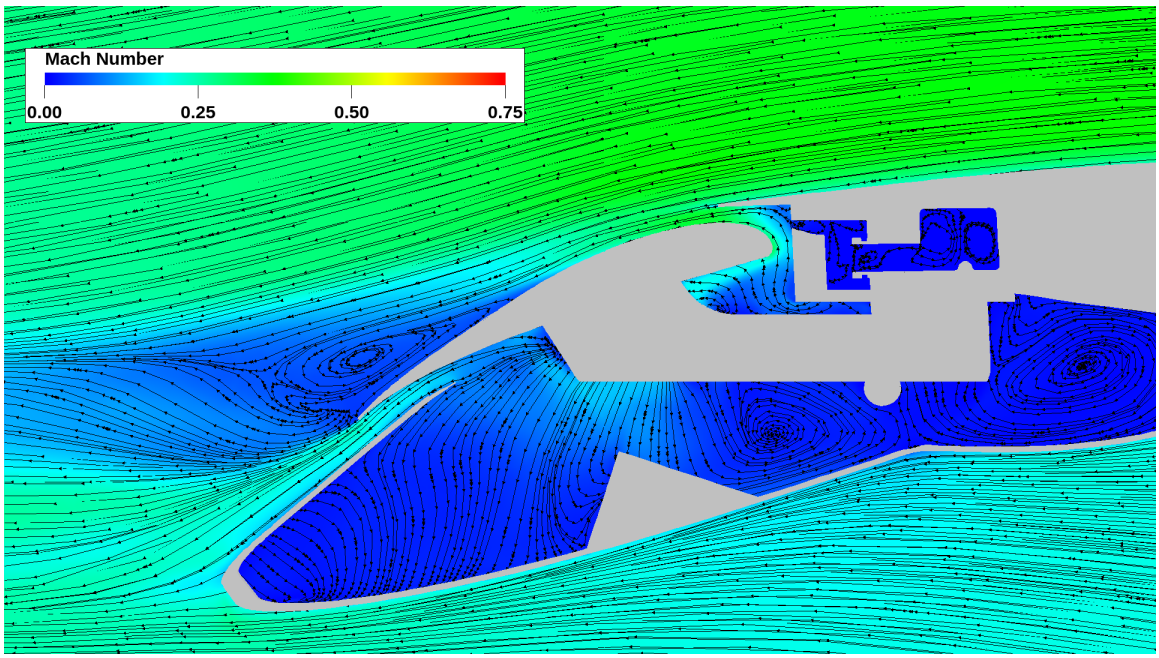

(a) AFC-OFF

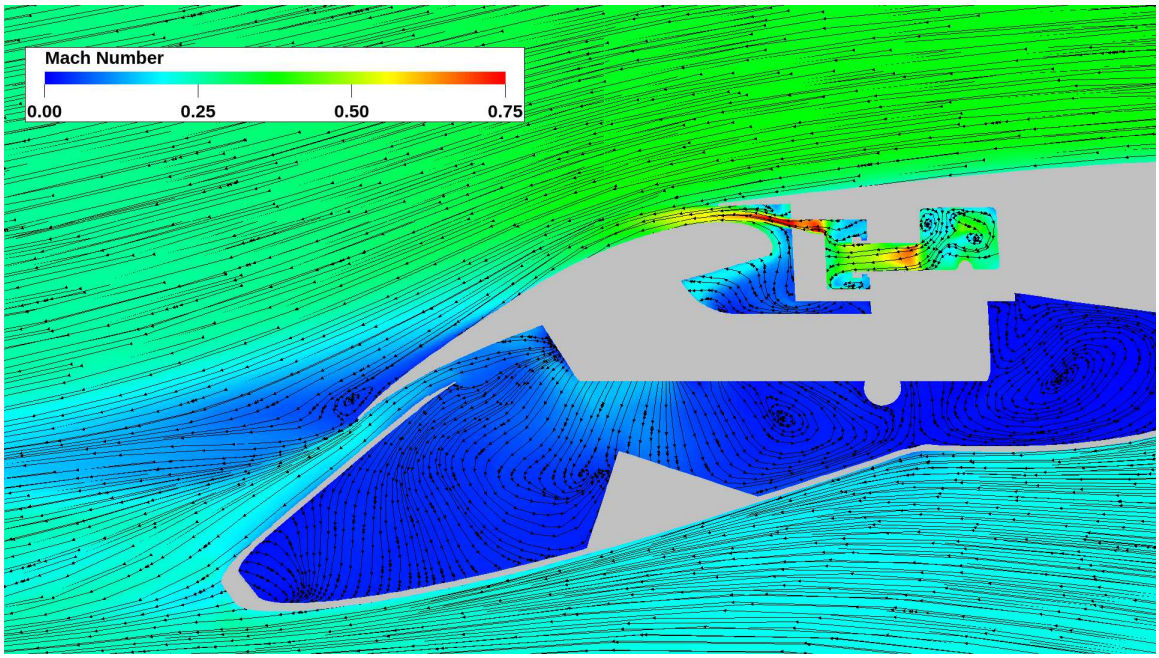

(b) AFC: FTPR=2.5

Fig. 20 Effect of LFGB AFC on off-surface flowfield at midwing section, Mach=0.26, $\alpha = 8°$, $Re = 4.24 \times 10^6$.